

## 22.56% total area efficiency of n-TOPCon solar cell with screen-printed Al paste



Yu Ding <sup>a</sup>, Lvzhou Li <sup>b</sup>, Haipeng Yin <sup>c</sup>, Xiuling Jiang <sup>c</sup>, Jianning Ding <sup>a,b,d,\*</sup>, Ningyi Yuan <sup>d,\*</sup>, Qin Qin Wang <sup>b,\*</sup>

<sup>a</sup> Institute of Intelligent Flexible Mechatronics, Jiangsu University, Zhenjiang 212013, PR China

<sup>b</sup> Institute of Technology for Carbon Neutralization, Yangzhou University, Yangzhou 225009, PR China

<sup>c</sup> R&D Innovation Center, JA Solar Technology Co. Ltd, Yangzhou 225000, PR China

<sup>d</sup> School of Materials Science and Engineering, Jiangsu Collaborative Innovation Center for Photovoltaic Science and Engineering, Jiangsu Province Cultivation Base for State Key Laboratory of Photovoltaic Science and Technology, Changzhou University, Changzhou 213164, Jiangsu, PR China

### ARTICLE INFO

#### Keywords:

n-TOPCon solar cell  
n<sup>+</sup>-Poly-Si layer  
Al paste  
Al-Si contact  
UV pulse laser

### ABSTRACT

Screen-printing Ag paste on the rear side of the Tunnel Oxide Passivated Contact solar cells (TOPCon) is still the mainstream method to form electrodes. However, the high price of precious metals increases the cost of TOPCon cells. Al is a cheap and high-performance conductor, and its work function is compatible with the rear side of TOPCon cells. In this study, we used a UV pulse laser (355 nm, 10 ps) to ablate the rear side SiN<sub>x</sub> passivation layer of TOPCon cells and then printed Al paste with different weight percentages of silicon (Si-wt.%) on the phosphorus-doped polycrystalline silicon (n<sup>+</sup>-poly-Si) layer to reduce the cost. We investigated the damage mechanism of laser on SiO<sub>x</sub>/n<sup>+</sup>-poly-Si/SiN<sub>x</sub> passivation structure and the contact mechanism between Al paste and n<sup>+</sup>-poly-Si layer. The results show that the  $V_{oc}$  of SiO<sub>x</sub>/n<sup>+</sup>-poly-Si/SiN<sub>x</sub> passivation structure reduced about 6–7 mV when the laser energy density was 0.431 J/cm<sup>2</sup>. We got the best electrical performance of TOPCon cells printed with Al paste (25 wt%–29 wt% silicon). The open-circuit voltage ( $V_{oc}$ ) and the conversion efficiency ( $E_{ff}$ ), have reached 663.60 mV and 22.56 % respectively. Although the efficiency was 9.40 % relative lower than that of TOPCon cells printed with Ag paste, but the cost of Al paste only accounted for 10 % of Ag paste. In the future, the highest  $E_{ff}$  of TOPCon solar cells printed with Al paste on the rear side are expected to reach the commercial TOPCon based on Ag paste, which applies laser doping selective emitter technology (SE) and bifacial poly-Si passivation structure.

### 1. Introduction

The rapid evolution of science and technology accelerates human development of new energy sources. Cz-Si wafers have the advantage of purity and carrier lifetime, so the photovoltaic (PV) devices based on Cz-Si wafers obtain high conversion efficiency [1]. Currently, the silicon solar cells include tunneling oxide passivation contact (TOPCon) [2], hetero-junction (HJT) [3] and integrated-back contact cells (IBC) [4] are been investigated widely. Among them, TOPCon solar cells has been commercial produced extensively due to its excellent passivation structure (SiO<sub>x</sub> + n<sup>+</sup>-poly-Si) and its low cost to upgrade the production lines from PERC solar cells.

TOPCon cells (Fig. 1) passivated by ultrathin SiO<sub>x</sub> with chemical passivation, and phosphorus-doped polycrystalline silicon (n<sup>+</sup>-poly-Si)

with electric field passivation [5–7], so the excellent passivation mechanism resulting the efficiency record of TOPCon cells refreshed consistently [2,6,8–12].

Improving efficiency and reducing costs are two key routes to lower the cost per kWh of TOPCon cells. In the whole TOPCon cells cost of ownership, apart from silicon wafers, the pastes used to form electrodes account for the largest proportion of the cost, especially, if full Ag paste printed on the rear side [2]. There are numerous reports on the formation mechanism of ohmic contact between Ag paste and n<sup>+</sup>-poly-Si [13–16]. However, there are few reports on printing Al paste on n<sup>+</sup>-poly-Si [17], and the contact mechanism of them is also not clear.

Therefore, the n-Type Cz-Si wafers were used in this study, and the solar cells were fabricated by commercial route. To inhibit the over-reaction between Al paste and n<sup>+</sup>-poly-Si, the glass which can burn

\* Corresponding authors at: Institute of Intelligent Flexible Mechatronics, Jiangsu University, Zhenjiang 212013, PR China (J. Ding).

E-mail addresses: [dingjin@ujs.edu.cn](mailto:dingjin@ujs.edu.cn) (J. Ding), [nyyuan@cczu.edu.cn](mailto:nyyuan@cczu.edu.cn) (N. Yuan), [wangqinqin@yzu.edu.cn](mailto:wangqinqin@yzu.edu.cn) (Q. Wang).

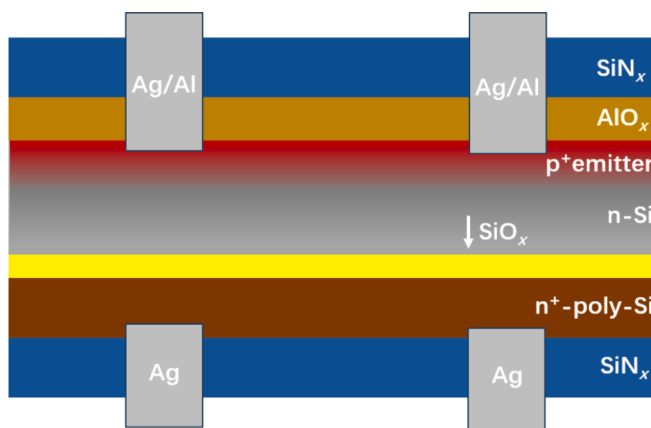


Fig. 1. Structural diagram of TOPCon solar cell [5].

through  $\text{SiN}_x$  was not added into Al paste, so the Laser Contact Opening (LCO) process for matching non-burn-through Al paste was researched. The interface morphology between Al paste (different weight percentages of silicon) and  $n^+$ -poly-Si was observed, not only that, the TOPCon cells electrical properties were analyzed to explain the contact mechanism between Al paste and  $n^+$ -poly-Si, and guide TOPCon cells on the path of cost reduction.

## 2. Experimental

### 2.1. Solar cell fabrication

The TOPCon cells were fabricated by 182 mm  $\times$  182 mm n-Type  $\text{Cz}_\text{Si}$  wafers with 1.0–1.3  $\Omega\text{-cm}$  resistivity, and the thickness of the wafers is about 140  $\mu\text{m}$ . The fabrication process is shown in Fig. 2, and the LCO step was added to the original process before printing Al paste on the rear side.

As shown in the flowchart, the wafers were textured in KOH solution to reduce the reflection of light in the front side firstly, then the front boron emitter ( $p^+$  emitter, 120  $\Omega/\text{sq}$ ) was formed in a quartz tube furnace in the atmosphere of  $\text{BCl}_3$  gas. After the  $p^+$  emitter was

fabricated, the rear side of the wafers was polished by HF and  $\text{HNO}_3$  mixed solution to remove the boron silicate glass (BSG) and the emitter on the rear side and the edges formed during boron diffusion. The rear side passivation contact structure, which consists of an ultrathin  $\text{SiO}_x$  (1.6 nm) layer and phosphorus-doped polycrystalline silicon (250 nm) layer, was formed by low-pressure chemical vapor deposition (LPCVD). Then, the phosphorous silicate glass (PSG) was single-sided etched with a volume ratio of 15 % HF solution in room temperature (25°C).  $\text{AlO}_x$  (7 nm) was fabricated by atomic layer deposition (ALD) in the front side of TOPCon cells to passivate the  $p^+$  emitter, because the  $\text{AlO}_x$  layer has a large amount of negative fixed charge to prevent the recombination of charge carriers. Finally, both sides of the silicon wafers passivated with  $\text{SiN}_x$  (70 nm), which was formed by LPCVD.

To form good contacts between Al paste and silicon wafers, a UV pulse laser ( $\lambda = 355 \text{ nm}$ ,  $PWM = 10 \text{ ps}$ ,  $f = 1 \text{ MHz}$ , size = 40  $\mu\text{m} \times 40 \mu\text{m}$ ) was used to ablate the rear side  $\text{SiN}_x$  in the metallization area with a speed of 10000 mm/s. The laser was tested with different energy densities which were regulated by changing the laser power to minimize the laser damage to silicon wafers (Table 1), and the laser energy density was calculated according to Formula (1).

$$D_{\text{energy}} = P/(f \times s) \quad (1)$$

In the end, Ag/Al paste and full Al paste were screen printed on the front side and rear side of the cells respectively, after that, the cells were sintered in a belt furnace with the curve shown in Fig. 3. The addition of silicon in Al paste can inhibit the violent reaction between Al paste and  $n^+$ -poly-Si, but also decreased the grids conductivity. Thus, the Al paste with different weight percentages of silicon was applied in metallization (Table 2).

### 2.2. Solar cell characterization

The open-circuit voltage ( $V_{oc}$ ), short-circuit current ( $I_{sc}$ ), series resistance ( $R_s$ ), fill factor (FF), and efficiency ( $E_{ff}$ ) of cells were measured by an IV tester under 1-sun illumination (AM 1.5). The implied  $V_{oc}$  ( $iV_{oc}$ ) and the dark saturation current density ( $J_0$ ) of the control samples were measured by a WCT-120 lifetime tester under the excess carrier density of  $3 \times 10^{15}$ . The transmission line method (TLM) model [18] was used to measure the line resistance and the contact resistivity ( $\rho_c$ ) of the electrode. Fig. 4 shows the schematic diagram of the TLM method, and the results can be obtained based on Formula (2):

$$R_{\text{measured}} = 2R_{\text{tip}} + 2R_c + R_s \quad (2)$$

$R_s$  is the bulk resistance of the  $n^+$ -poly-Si layer. The  $R_{\text{tip}}$  which represents the resistance between the probe and the metal grids, is the same on the same grid. Meanwhile, bulk resistance  $R_s$  can be represented by sheet resistance  $R_{\text{sheet}}$ , so Formula (2) can be simplified as Formula (3):

$$R_{\text{measured}} = 2R_c + (R_{\text{sheet}} \times d)/w \quad (3)$$

Photoluminescence (PL) images and the loss of  $iV_{oc}$  ( $\Delta iV_{oc}$ ) are used as an indication of damage after LCO. In addition, the microstructure was observed by scanning electron microscope (SEM) and energy dispersive spectrometer (EDS) to evaluate the ablation state of the  $\text{SiN}_x$  passivation layer. Moreover, the contact interface of Al paste and  $n^+$ -poly-Si was analyzed by SEM and EDS as well.

Table 1  
LCO parameters adopted in this study.

Power/W	Energy Density/ $\text{J}\cdot\text{cm}^{-2}$
6.3	0.394
6.6	0.413
6.9	0.431
7.2	0.450
7.5	0.469

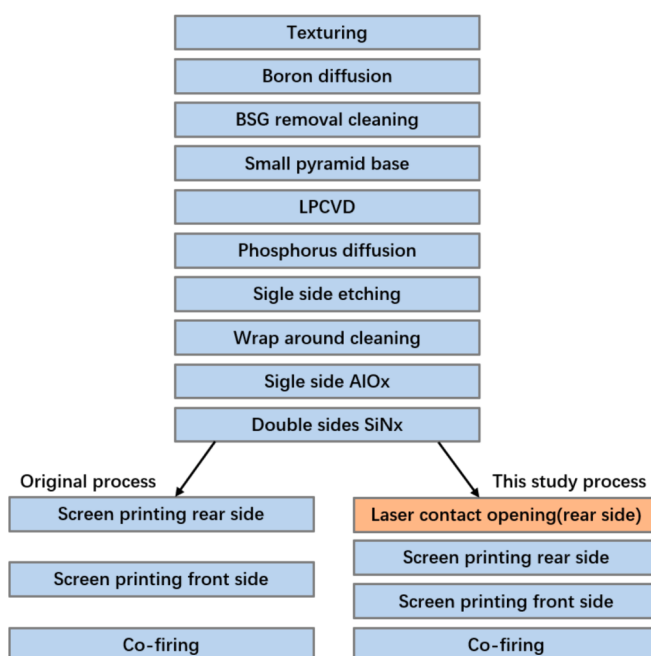


Fig. 2. Fabrication process of TOPCon cells.

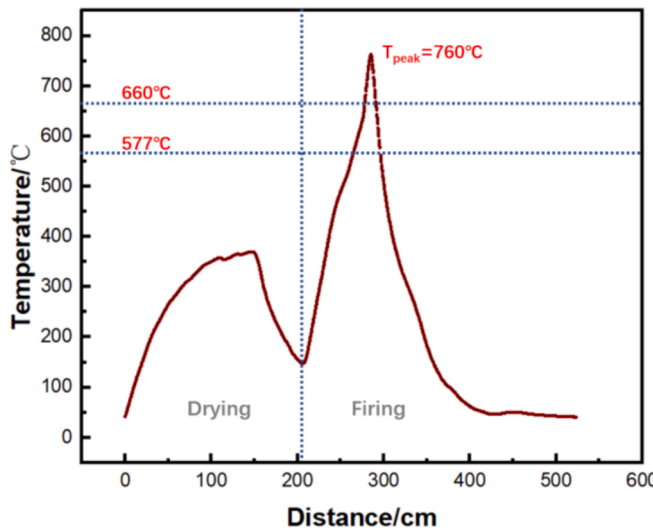


Fig. 3. Sintering temperature curve.

**Table 2**  
The Al paste with different weight percentages of silicon.

Bath		Silicon contents/wt.%
jLow Si-wt.%	sp1	1–5
	sp2	9–13
High Si-wt.%	sp3	18–23
	sp4	25–29

### 3. Results and discussion

#### 3.1. Effects of the laser with different energy densities on $\text{SiO}_x/\text{n}^+\text{-poly-Si/SiN}_x$ structure

The silicon wafer was divided into six regions, Fig. 5a is the PL image of the silicon wafer after the laser ablated with different energy densities, and the loss of  $iV_{oc}$  ( $\Delta iV_{oc}$ ) is marked on Fig. 5b.

As shown in Fig. 5b,  $\Delta iV_{oc}$  raised with the increase of laser energy density. When laser energy density is lower than  $0.413 \text{ J}\cdot\text{cm}^{-2}$  or higher than  $0.431 \text{ J}\cdot\text{cm}^{-2}$ , the increase rates of  $\Delta iV_{oc}$  all less than 15 %. However, when the laser energy density increased from  $0.413 \text{ J}\cdot\text{cm}^{-2}$  to  $0.431 \text{ J}\cdot\text{cm}^{-2}$ , the  $\Delta iV_{oc}$  increased from  $4.97 \text{ mV}$  to  $6.20 \text{ mV}$  with up to 25 % growth rate, the effect of laser on  $\text{SiO}_x/\text{n}^+\text{-poly-Si/SiN}_x$  structure has undergone a qualitative change during this period. Moreover, the contact interface of Al paste and  $\text{n}^+\text{-poly-Si}$  was analyzed by SEM and EDS as well.

When a laser energy density lower than  $0.431 \text{ J}\cdot\text{cm}^{-2}$  was not sufficient to open the  $\text{SiN}_x$  layer, because the energy density was too little low to reach the laser ablation threshold, and the EDS results proved it. When laser energy density is higher than  $0.431 \text{ J}\cdot\text{cm}^{-2}$ , large areas of  $\text{n}^+\text{-poly-Si}$  exposed after laser-radiated, because no nitrogen element appeared in the area. From Fig. 6, we find that there are many cracks at the edge of the  $\text{SiN}_x$  layer after ablation, which is created by the mechanical stress caused by  $\text{n}^+\text{-poly-Si}$  and  $\text{SiN}_x$ .

Since during laser ablation, the absorption coefficient( $\alpha$ ) of  $\text{n}^+\text{-poly-Si}$  at  $355 \text{ nm}$  wavelength is several orders of magnitude larger than that of  $\text{SiN}_x$  [19,20], the  $\text{n}^+\text{-poly-Si}$  layer obtained large energy from the laser, resulting in the temperature increased to the melting point of  $\text{n}^+\text{-poly-Si}$ , therefore, a phase transformation (solid  $\rightarrow$  liquid) occurred in  $\text{n}^+\text{-poly-Si}$  under laser radiation regions, and the vapor pressure caused by the phase transformation broke down the  $\text{SiN}_x$  above. Due to the

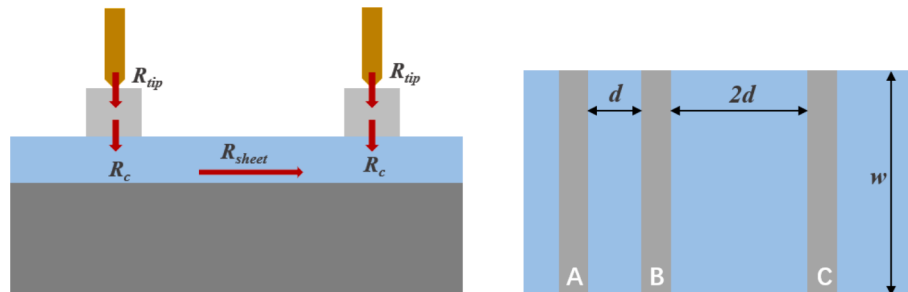


Fig. 4. The schematic diagram of TLM.

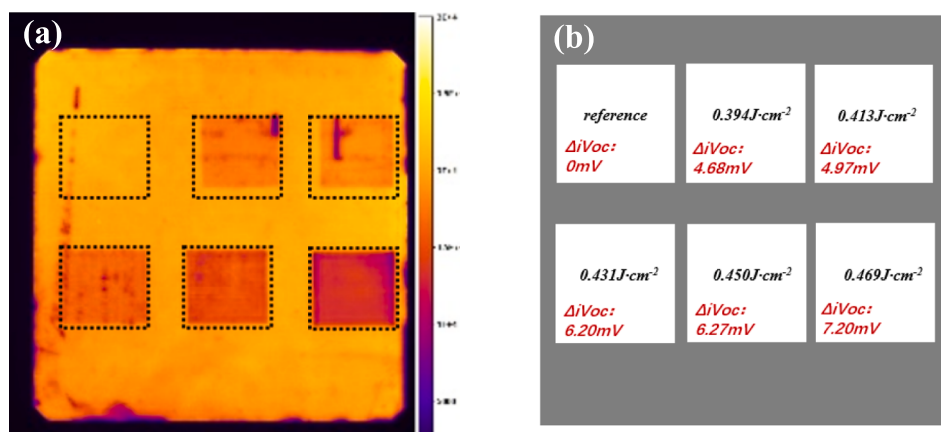
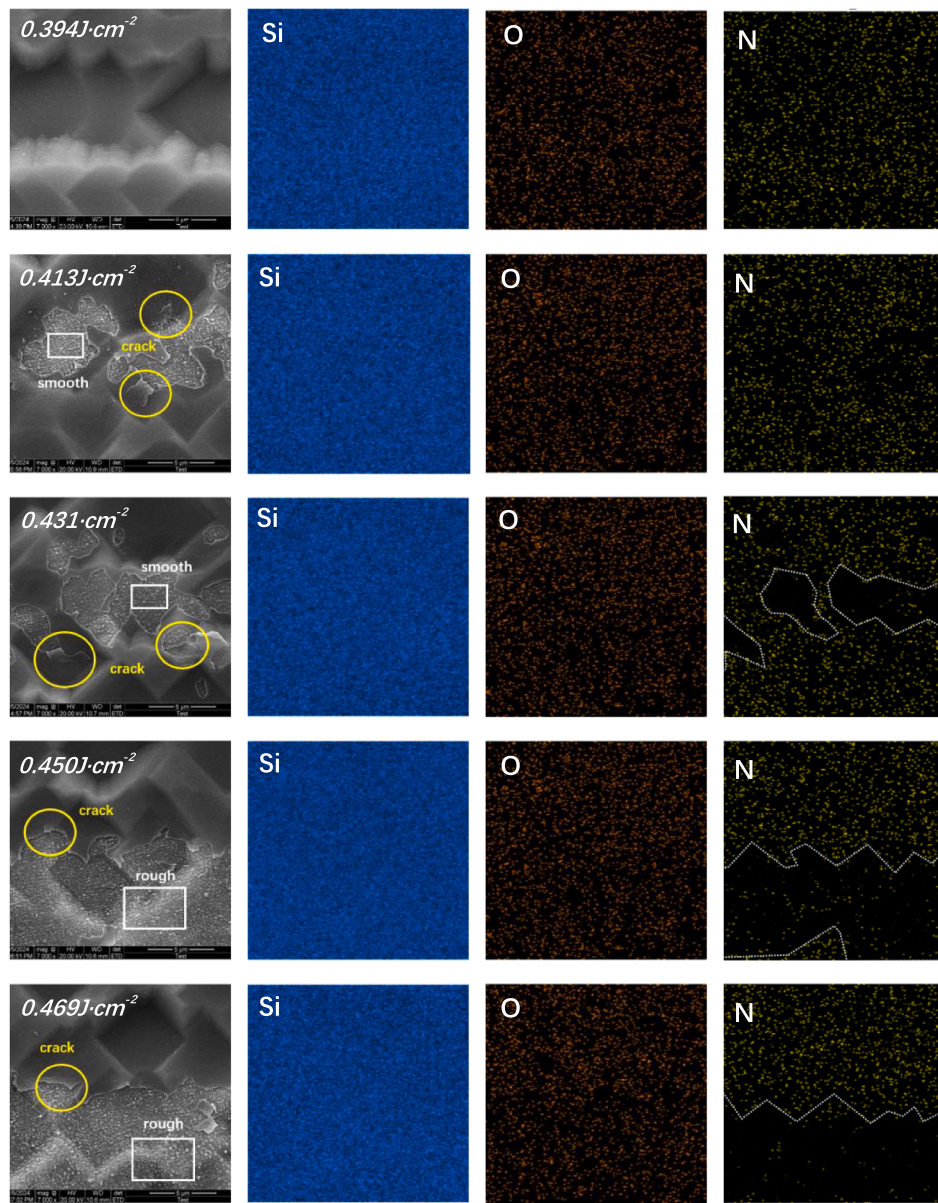


Fig. 5. (a) PL image of the silicon wafer after laser ablation with different energy densities and (b) shows the  $\Delta iV_{oc}$  affected by the laser with different energy densities in correspondent regions.



**Fig. 6.** Microstructure morphology observed by SEM and element distribution analyzed by EDS over the regions after laser ablated.

short laser pulse time (10 ps), the melted n<sup>+</sup>-poly-Si recrystallized and solidified into its original state (liquid → solid) rapidly.

The rough surface (white box region in Fig. 6) was the result of n<sup>+</sup>-poly-Si recrystallization, larger energy density laser led to deeper n<sup>+</sup>-poly-Si recrystallization, as a result, the defects caused by recrystallization brought more carriers recombination, which may explain the trend of  $\Delta iV_{oc}$  changes under different laser energy densities effectively. Therefore, the threshold of laser energy density is 0.431 J·cm<sup>-2</sup> when the UV picosecond laser worked on the structure of SiO<sub>x</sub>(1.6 nm)/n<sup>+</sup>-poly-Si(250 nm)/SiN<sub>x</sub>(70 nm). Hence, all the silicon wafers in metallization dealt with the laser energy density of 0.431 J·cm<sup>-2</sup>.

### 3.2. Study of the mechanism of Al-Si contact

The rear side SiN<sub>x</sub> passivation layer in metallization regions was ablated by the laser with 0.431 J·cm<sup>-2</sup>. The Ag/Al paste and the Al paste with different silicon weight percentages were screen printed on the front side and rear side of TOPCon cells respectively. In order to achieve a good metal-semiconductor contact, all the silicon wafers were sintered in industrial belt furnace, the actual sintering temperature cure is shown

in Fig. 3, the peak temperature was 760°C, which is higher than the melting point of Al (660°C). In order to reveal the mechanism of Al-Si contact, we analyzed the Al-Si contact interface on the basis of the Al-Si binary phase diagram (Fig. S1) [21].

The formation of ohmic contact is closely related to the Al-Si alloying process [22]. The process can be divided into three stages. In the first stage, Al particles in the paste melt slowly and the silicon from paste or n<sup>+</sup>-poly-Si dissolved in melted Al as the temperature increases (A→B→C). The second stage is the saturation of silicon dissolved in Al-Si alloy melt occurring at point C ( $T_{peak}$ ), and the process lasts for a short time usually. The final stage is the decrease of temperature, during the cooling process of the melt, the solubility of silicon in Al-Si alloy melt decreases, which leads to more silicon precipitate from the melt to form a back surface field (BSF), as a result, the amount of the silicon precipitation affected the thickness of BSF closely.

The eutectic temperature of Al-Si is about 577°C, which means that a eutectic reaction happens between Al and Si at this temperature ( $l \rightarrow \alpha + \beta$ ). When the content of silicon involved in the reaction is between 1.65 % to 12.6 %, the primary phase  $\alpha$  (Si-Al solid solution) precipitates slowly with the temperature decreases. When the temperature cools

down to eutectic temperature (577°C), the remaining liquid undergoes eutectic reaction ( $L_{\text{remain}} \rightarrow \alpha + \beta$ ). However, the solid solubility of Si in Al decreases when the temperature drops below 577°C, at this time, the excessive Si in  $\alpha$  phase segregates in the form of the second phase  $\beta_{\text{II}}$ , so the final Al-Si hypoeutectic alloy composed of  $\alpha + \beta + \beta_{\text{II}}$ . However, when silicon content is between 12.6 % to 99.83 %, the Al-Si is hyper-eutectic alloy, which is in contrast to hypoeutectic. When the temperature drops to room temperature, excessive Al segregates from the primary phase  $\beta$  (Al-Si solid solution) in the form of the second phase  $\alpha_{\text{II}}$ , so  $\alpha + \beta + \alpha_{\text{II}}$  constitute Al-Si hypereutectic alloy at room temperature.

To indicate the sintering process, Fig. 8(e–f) shows the schematics of Al-Si contacts, if no silicon was added to the Al paste, the Al melt reacted with  $n^+$ -poly-Si and the TOPCon structure would be destroyed.

To protect the passivation structure, different weight percentages of silicon were added into the Al paste, so the Al melt reacted with the silicon from the paste first, and less from  $n^+$ -poly-Si diffused into the melt. The microscopic morphology and schematic of the cross-section at the Al-Si contact interface as shown in Figs. 7 and 8 (e–f), when the weight percentage of silicon in Al paste lower than 18 %, there was a clear interlayer between Al-Si alloy and silicon bulk, which caused by the formed of Al-Si solid solutions ( $\beta$  phase, BSF).

The thickness of BSF decreased with the increasing silicon weight percentage in Al paste, when the added silicon was 1 wt%–5 wt%, the thickness of BSF was 3.67  $\mu\text{m}$ , and when the silicon in Al paste increased to 9 wt%–13 wt%, the thickness decreased to 3.14  $\mu\text{m}$ . However, the total thickness of passivation layers was about 250 nm, so the TOPCon structure was destroyed obviously, and when the silicon in Al paste over 18 wt%, no BSF was observed at the interface. In addition, many voids (the regions marked with yellow circles) appeared in Al-Si alloy, Lauermann et al. [23] found that the diffusion occurring at 20°C less than the peak temperature tends to dominate the entire diffusion process, in addition the diffusion speed of Si is greater than that of Al,

therefore, the silicon in Al-Si alloy transfer to the Al layers occurred in the process, which led to the reduction of the silicon content in the melt, and more and more silicon from  $n^+$ -poly-Si diffused to the melt to maintain phase balance. So, the voids formed in the alloy when the silicon diffused and the melt flow.

The shape of metal grids can also affect the performance of solar cells, the aspect ratio (height/width) is used to indicate the performance of the grid after sintering, higher aspect ratio leads to smaller series resistance. In addition, the higher aspect ratio grids decrease the shielded area of light.

The aspect ratio of the grids was measured by a confocal scanning laser microscope (Fig. 8(a–d)). The Al paste with a low weight percentage of silicon formed higher aspect ratio grids, because most silicon reached Al melt from  $n^+$ -poly-Si, even the temperature reached Al melting temperature, but the high-temperature duration was too short, so the Al particles didn't obtain enough energy to melt, and the grids maintain the original morphology without collapse.

On the contrary side, the Al paste with a higher weight percentage of silicon provided enough silicon for Al particles to form Al-Si alloy, therefore, all the Al particles reacted during the sintering process, and led to the grids collapsing, which decreased the aspect ratio. The wafers almost not participate in the reaction, therefore, no silicon diffusion occurred in  $n^+$ -poly-Si, and no voids formed in the Al-Si alloy. As a result, the size of the metal particles in high silicon weight percentage paste (Fig. 7(c) (d)) is larger than that of the metal particles in lower silicon weight percentage paste (Fig. 7(a) (b)) after sintering.

### 3.3. Impact of different silicon weight percentages in Al paste on cell performance

The metallization process affected cell performance highly, Table 3 lists the line resistance and contact resistivity of metal grids measured by

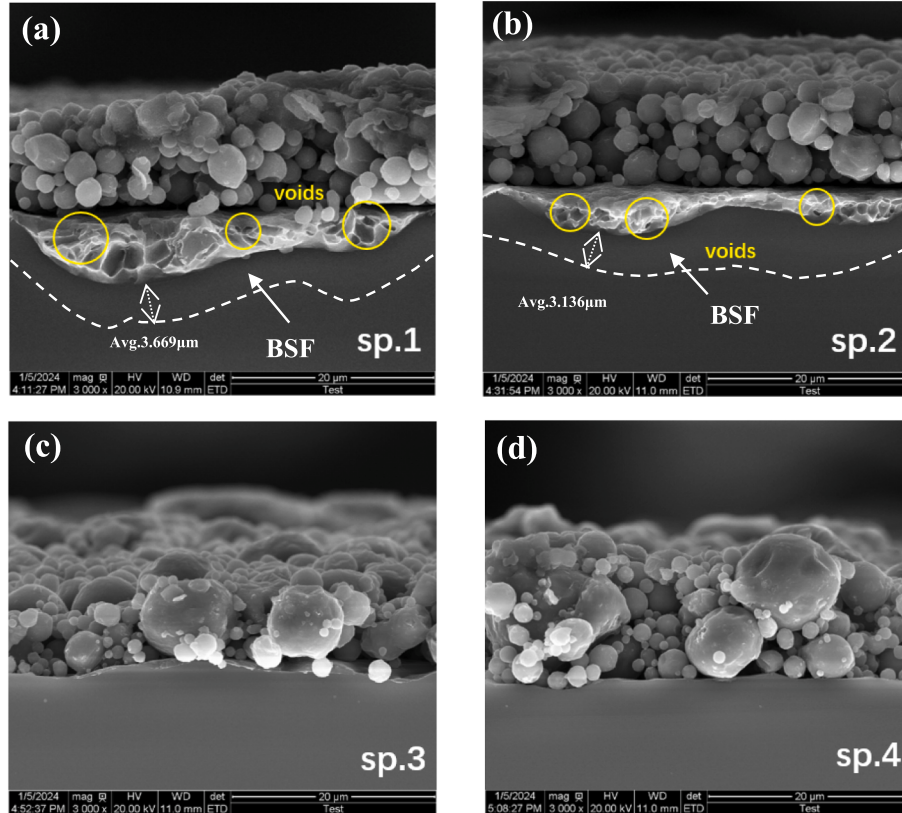


**Fig. 7.** SEM images of the cross-section of Al-Si contact: (a) the silicon content in Al paste is 1 wt%–5 wt%; (b) 9 wt%–13 wt%; (c) 18 wt%–23 wt%; (d) 25 wt%–29 wt%.

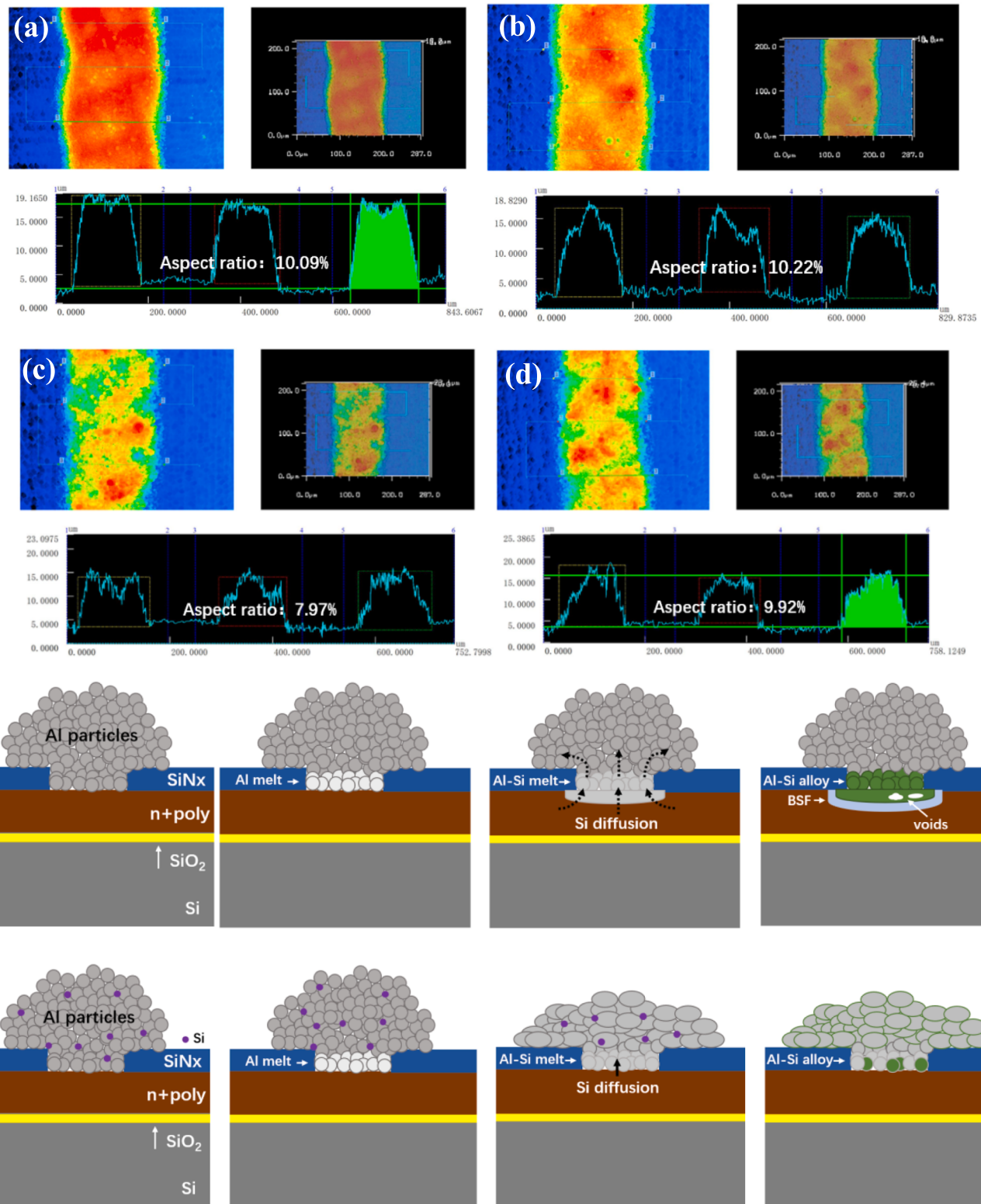


**Fig. 8.** SEM images of the cross-section of the Al-Si contact: (a) the silicon content in Al paste is 1 wt%–5 wt%; (b) 9 wt%–13 wt%; (c) 18 wt%–23 wt%; (d) 25 wt%–29 wt%. (e) and (f) are the schematics of the Al-Si contact with different silicon weight percentages in Al paste: (e) no silicon in Al paste; (f) high silicon contents in Al paste.

#### TLM.

The table values indicate that more silicon addition decreased the conductivity of grids, but reduced the contact resistivity. However, the contact resistivity trend is contradictory to the cross-section images in Fig. 7.

As we know, ohmic contact was established with the formation of Al-Si alloy, and Al-Si alloy thickness decreased with the weight percentage of silicon in Al paste increase. Combing with the TLM model, we find that, the test current only goes through  $n^+$ -poly-Si during lateral transmission in ideal cells, but in fact, the passivation structure ( $SiO_x/n^+$ -

**Table 3**

Line resistance and contact resistivity of metal grids.

Silicon contents (wt.%)	Line resistance (Ohm/cm)	Contact resistivity (mOhm·cm <sup>2</sup> )
1–5	2.2768	8.062
9–13	2.2296	10.582
18–23	7.1986	5.682
25–29	8.9896	3.831

poly-Si) was destroyed when the cells printed with low silicon added Al paste, which led to the test current had  $n^+$ -poly-Si and Cz-Si bulk two paths to go through during lateral transmission. In this case, the  $R_c$  in Formula (3) represents the contact resistance between grids and Cz-Si bulk.

The metal–semiconductor contact influenced the fill factor (FF), open-circuit voltage ( $V_{oc}$ ), short-circuit current ( $I_{sc}$ ), and efficiency ( $E_{ff}$ ). Fig. 9 describes the performance of the TOPCon cells printed with Al paste on the rear side.

Results show that, the  $I_{sc}$  has an obvious decreasing trend when the weight percentage of silicon increased. The Al-Si contact interface affected long wave light absorption (900 nm–1000 nm) on the rear side. Fig. S3 is the EQE of the cells, which indicates that the cells printed with high Si-wt.% added Al paste had a stronger response at long wave than that of printed with lower Si-wt.% added Al paste. Reasonably, the strong response in long wave can increase the  $I_{sc}$ , but the EQE curve indicates that these differences are small, so the increasement on the  $I_{sc}$

can be ignored. However, there is no doubt that, the increasing Si content in paste makes line resistance higher, resulting in decreasing  $I_{sc}$ , the line resistances are listed in Table 3. According to the description in Section 3.2, the Al paste with low Si-wt.% addition contacted with  $n^+$ -poly-Si formed thick Al-Si alloy on the rear side, which affected  $J_{0,metal}$  seriously. In this study, we can calculate  $J_{0,metal}$  by Formula (4) [24].

$$J_{0,\text{total}} = J_{0,\text{bulk}} + J_{0,\text{metal}(F)} \times f_{(F)} + J_{0,\text{passivation}(F)} \times (1 - f_{(F)}) + J_{0,\text{metal}(R)} \times f_{(R)} + J_{0,\text{passivation}(R)} \times (1 - f_{(R)}) \quad (4)$$

$J_{0,\text{total}}$ , the total dark saturation current density of the cells can be expressed by formula(4), which is composed of bulk saturation current density  $J_{0,\text{bulk}}$  and surface dark saturation current density, and the values of  $J_{0,\text{total}}$  can be measured by WCT-120(SunsVoc). The surface is divided into front and rear sides, and each side is further subdivided into metallization and non-metallization regions. In formula (4),  $J_{0,\text{passivation}}$  represents the dark saturation current density in non-metallization regions, and R and F represent the rear side and front side respectively. The  $J_{0,\text{total}}$  of the cells printed with different Si-wt.% added Al paste (from low to high) are 411fA/cm<sup>2</sup>, 381fA/cm<sup>2</sup>, 315fA/cm<sup>2</sup> and 275fA/cm<sup>2</sup> measured by WCT-120(SunsVoc) respectively. Fig. S4 shows the remaining values involved in Formula (4), all the values are measured by WCT-120(Lifetime) (the testing methods in Section2.2) from our previous offline experiments. Specifically,  $J_{0,\text{bulk}}$  cannot be obtained from measurement directly, we obtained  $J_{0,\text{bulk}}$  by Formula (5).

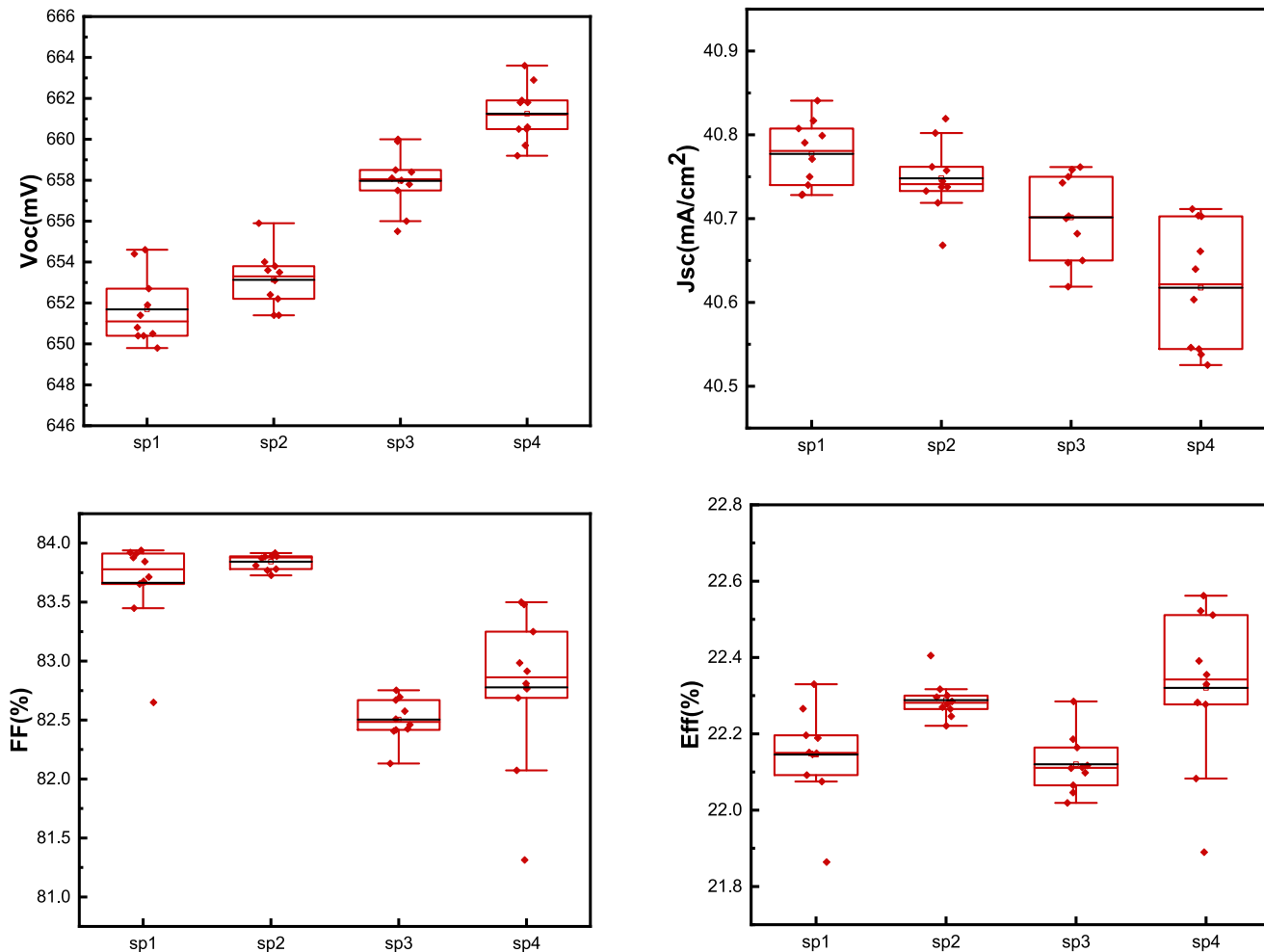


Fig. 9. The performance of TOPCon cells printed with different weight percentages of silicon added Al paste (sp1:1–5 wt%; sp2:9–13 wt%; sp3:18–23 wt%; sp4:25–29 wt%).

$$J_0 = qWn_i^2/\tau N_d \quad (5)$$

Which  $J_0$  represents  $J_{0,\text{bulk}}$ , and  $q = 1.6\text{E-19}$ , which is constant.  $W$  is the thickness of Si wafers,  $n_i = 8.89\text{E}9\text{cm}^3$  represents the electron concentration of intrinsic silicon in 300 K [25].  $\tau = 3500 \mu\text{s}$  is the minority carrier life time of Si wafers (measured by WCT-120),  $N_d = 1\text{E}16$  represents the P doping concentration in n-type Si wafers. So, the value of  $J_{0,\text{bulk}}$  is  $5\text{fA/cm}^2$  can be obtained by formula 5. According to calculations, the  $J_{0,\text{metal}}$  values are  $4955.16\text{fA/cm}^2$ ,  $4575.42\text{fA/cm}^2$ ,  $3739.97\text{fA/cm}^2$  and  $3233.65\text{fA/cm}^2$  respectively.

The  $V_{oc}$  enhanced with the increase of the weight percentage of silicon in Al paste, but the champion  $V_{oc}$  was much worse than that of the cells printed Ag paste on the rear side [26]. This is because, the appearance of BSF built an electric field, which weakened the electric field passivation of  $n^+$ -poly-Si and inhibited the transfer of major carriers (electrons) to the rear side grids. Fig. 10 describes the transfer of charge carriers in the cells,  $n^+$ -poly-Si provided a built-in field with the direction from  $n^+$ -poly-Si to silicon bulk, which was beneficial for the rear side electrode to collect charge carriers. However, the appearance of BSF weakened the ability of electrodes, because the BSF showed p-type semiconductor properties, so a built-in field with the direction from BSF to  $n^+$ -poly-Si formed by it, which led to most major carriers recombined. As a consequence, the decrease of  $J_{0,\text{metal}}$  promotes the increase in  $V_{oc}$ , and in this study, the champion  $V_{oc}$  was 663.6 mV and the efficiency was 22.56 %. Fig. 11 shows the IV current of the champion solar cell.

#### 4. Failure analysis and outlook

Table 4 compares the IV test results of TOPCon cells which printed Ag paste and Al paste on the rear side respectively. Obviously, there is a large gap in  $V_{oc}$  of the cells, the  $V_{oc}$  of TOPCon cells printed with Al paste on the rear side is 7.8 % smaller than that of TOPCon cells printed with Ag paste on the rear side, and the cause of this difference has been explained in Chapter 3.3. So far, printing Al paste on TOPCon cells' rear side can reduce the costs, but the efficiency cannot match that of TOPCon cells printed with Ag paste. I believe that in the future, the optimization of laser contact opening technology and the superposition of LECO, the  $V_{oc}$  of TOPCon cells which are printed with Al paste on the rear side can be improved partly. Our next work will focus on the impact of the reverse electric field on the rear side.

#### 5. Conclusion

This work is dedicated to the development of a new metallization process to reduce the cost of commercial TOPCon solar cells, including laser contact opening (LCO) and screen-printing Al paste on TOPCon cells' rear side. The results revealed that the laser energy density affected  $\text{SiO}_x/n^+$ -poly-Si/ $\text{SiN}_x$  structure passivation, when we used a UV picosecond laser (355 nm, 10 ps) with an energy density of  $0.431 \text{ J/cm}^2$ , the laser caused the least damage to  $\text{SiO}_x/n^+$ -poly-Si/ $\text{SiN}_x$  structure

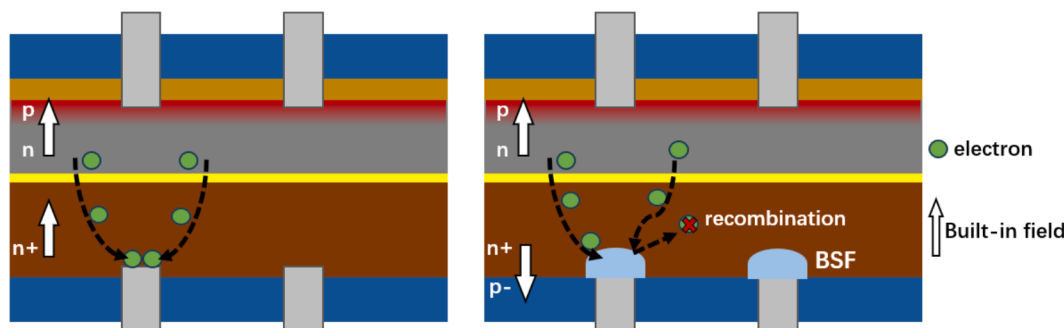


Fig. 10. Schematic of the majority carriers on TOPCon cells' rear side with and without BSF.

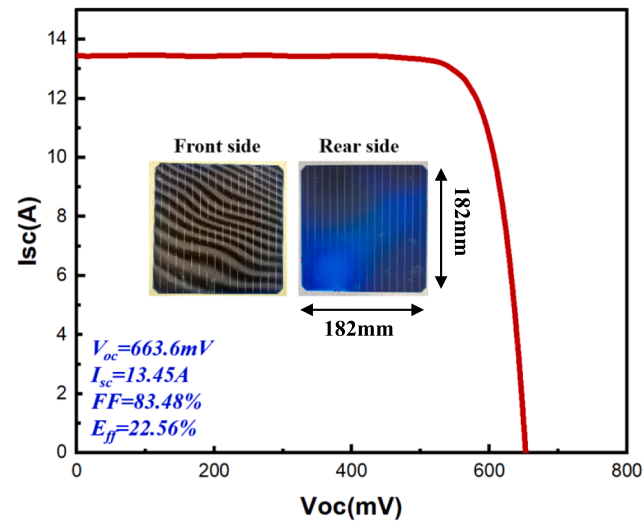


Fig. 11. The  $I$ - $V$  curve of the champion TOPCon solar cell in this work.

Table 4

The  $I$ - $V$  results of the TOPCon cells printed Ag paste and Al paste on the rear side.

Rear side	$I_{sc}$ (A)	$V_{oc}$ (mV)	FF (%)	$E_{ff}$ (%)
Ag paste	13.87	716.6	83.55	24.63
Al paste	13.46	661.3	82.78	22.32

(about 4.97 mV).

The weight percentage of silicon in the Al paste affected the contact interface of  $n^+$ -poly-Si and grids, the Al paste with a low weight percentage of silicon caused many voids and thick Al-Si alloy, which brought more metal recombination ( $J_{0,\text{metal}}$ ) in metallization regions. In addition, the formation of BSF caused by Al-Si alloy decreased  $V_{oc}$  of the cells as well, because the built-in field caused by BSF inhibited the carriers transport and brought more recombination. The Al paste with a high weight percentage of silicon hardly had these situations, so the cells printed with high Si-wt.% added Al paste showed better electrical performance, the champion TOPCon cell obtained when printed with the Al paste which has 25-29 wt% silicon, and the cell with  $V_{oc}$  663.6 mV,  $I_{sc}$  40.73 mA/cm<sup>2</sup>, FF 83.48 %, and  $E_{ff}$  22.56 %.

Although there is a significant gap in efficiency between TOPCon cells printed with Al paste and Ag paste on the rear side, the use of Al paste on TOPCon cells' rear side has large economic benefits for commercialization. To improve the  $V_{oc}$  of TOPCon cells which are printed with Al paste on the rear side, the LCO technology optimization, selective emitter (SE) technology, and laser enhanced contact optimization (LECO) technology will be applied in our future work.

## CRediT authorship contribution statement

**Yu Ding:** Writing – original draft, Methodology, Investigation, Data curation. **Lvzhou Li:** Investigation. **Haipeng Yin:** Formal analysis, Data curation. **Xiuling Jiang:** Investigation, Formal analysis. **Jianning Ding:** Writing – review & editing, Supervision, Resources, Funding acquisition, Conceptualization. **Ningyi Yuan:** Writing – review & editing. **Qinqin Wang:** Writing – review & editing, Investigation, Formal analysis.

## Declaration of competing interest

The authors declare that they have no known competing financial interests or personal relationships that could have appeared to influence the work reported in this paper.

## Acknowledgements

This work has been partially supported by the Special Fund for Science and Technology Innovation of Jiangsu Province (BE2022022-4), National Natural Science Foundation youth project (62304199).

## Appendix A. Supplementary data

Supplementary data to this article can be found online at <https://doi.org/10.1016/j.solener.2024.112862>.

## References

- [1] S. Kashyap, J. Madan, R. Pandey, J. Ramanujam, 22.8% efficient ion implanted PERC solar cell with a roadmap to achieve 23.5% efficiency: a process and device simulation study, *Opt. Mater.* 128 (2022).
- [2] Z.-B. Liu, Z.-W. Li, C.-L. Guo, Y. Liu, H.-P. Peng, J.-H. Wang, X.-P. Su, Effect of firing process on electrical properties and efficiency of n-TOPCon solar cells, *Sol. Energy* 267 (2024).
- [3] L. Wen, L. Zhao, G. Wang, X. Jia, X. Xu, S. Qu, X. Li, X. Zhang, K. Xin, J. Xiao, W. Wang, Beyond 25% efficient crystalline silicon heterojunction solar cells with hydrogenated amorphous silicon oxide stacked passivation layers for rear emitter, *Sol. Energy Mater. Sol. Cells* 258 (2023).
- [4] P. Wang, R. Sridharan, X.R. Ng, J.W. Ho, R. Stangl, Development of TOPCon tunnel-IBC solar cells with screen-printed fire-through contacts by laser patterning, *Sol. Energy Mater. Sol. Cells* 220 (2021).
- [5] N. Lin, Z. Yang, H. Du, Z. Ding, Z. Liu, H. Xing, M. Xiao, Y. Ou, W. Liu, M. Liao, B. Yan, S. Huang, Y. Zeng, J. Ye, Excellent surface passivation of p-type TOPCon enabled by ozone-gas oxidation with a single-sided saturation current density of ~4.5 fA/cm<sup>2</sup>, *Sol. Energy* 259 (2023) 348–355.
- [6] H. Du, T. Wang, W. Liu, Y. Ou, M. Xing, W. Yang, J. Sheng, M. Liao, Z. Gu, B. Yan, Z. Yang, Y. Zeng, J. Ye, 24.18% efficiency TOPCon solar cells enabled by super hydrophilic carbon-doped polysilicon films combined with plated metal fingers, *Sol. Energy Mater. Sol. Cells* 257 (2023).
- [7] Z. Liu, N. Lin, Q. Zhang, B. Yang, L. Xie, Y. Chen, W. Li, M. Liao, H. Chen, W. Liu, Y. Wang, S. Huang, B. Yan, Y. Zeng, Y. Wan, J. Ye, 24.4% industrial tunnel oxide passivated contact solar cells with ozone-gas oxidation Nano SiO<sub>x</sub> and tube PECVD prepared in-situ doped polysilicon, *Sol. Energy Mater. Sol. Cells* 243 (2022).
- [8] J. Xu, C. Chen, C. Liu, J. Chen, Z. Liu, X. Yuan, H. Li, High efficiency TOPCon solar cells with micron/nano-structured emitter for a balance of light-trapping and surface passivation, *Sol. Energy Mater. Sol. Cells* 238 (2022).
- [9] Z. Liu, Z. Yang, W. Wang, Q. Yang, Q. Han, D. Ma, H. Cheng, Y. Lin, J. Zheng, W. Liu, M. Liao, H. Chen, Y. Wang, Y. Zeng, B. Yan, J. Ye, Numerical and experimental exploration towards a 26% efficiency rear-junction n-type silicon solar cell with front local-area and rear full-area polysilicon passivated contacts, *Sol. Energy* 221 (2021) 1–9.
- [10] M.Q. Khokhar, S. Chowdhury, D.P. Pham, S.Q. Hussain, E.-C. Cho, J. Yi, Improving passivation properties using a nano-crystalline silicon oxide layer for high-efficiency TOPCon cells, *Infrared Phys. Technol.* 115 (2021).
- [11] D. Chen, Y. Chen, Z. Wang, J. Gong, C. Liu, Y. Zou, Y. He, Y. Wang, L. Yuan, W. Lin, R. Xia, L. Yin, X. Zhang, G. Xu, Y. Yang, H. Shen, Z. Feng, P.P. Altermatt, P. J. Verlinden, 24.58% total area efficiency of screen-printed, large area industrial silicon solar cells with the tunnel oxide passivated contacts (i-TOPCon) design, *Sol. Energy Mater. Sol. Cells* 206 (2020).
- [12] C. Quan, Y. Zeng, D. Wang, M. Liao, H. Tong, Z. Yang, Z. Yuan, P. Gao, B. Yan, K. Chen, J. Ye, Computational analysis of a high-efficiency tunnel oxide passivated contact (TOPCon) solar cell with a low-work-function electron-selective-collection layer, *Sol. Energy* 170 (2018) 780–787.
- [13] S. Tepner, A. Lorenz, Printing technologies for silicon solar cell metallization: A comprehensive review, *Prog. Photovolt. Res. Appl.* 31 (2023) 557–590.
- [14] J.-T. Tsai, L.-K. Lin, S.-T. Lin, L. Stanciu, M.-B.-G. Jun, The influence of Bi<sub>2</sub>O<sub>3</sub> glass powder in the silver paste and the impact on silicon solar cell substrates, *Mater. Des.* 200 (2021).
- [15] A.A. Wereszczak, M.C. Modugno, B.R. Chen, W.M. Carty, Contact drying of printed sinterable-silver paste, *IEEE Trans. Compon. Packag. Manuf. Technol.* 7 (2017) 2079–2086.
- [16] S. Körner, F. Kiefer, R. Peibst, F. Heinemeyer, J. Krügener, M. Eberstein, Basic study on the influence of glass composition and aluminum content on the Ag/Al paste contact formation to boron emitters, *Energy Procedia* 67 (2015) 20–30.
- [17] D. Ourinson, A. Brand, A. Lorenz, M. Dhamrin, S. Tepner, M. Linse, N. Göttlicher, R. Haberstroh, K. Tsuji, J.D. Huyeng, F. Clement, Paste-based silver reduction for iTOPCon rear side metallization, *Sol. Energy Mater. Sol. Cells* 266 (2024).
- [18] S. Guo, G. Gregory, A.M. Gabor, W.V. Schoenfeld, K.O. Davis, Detailed investigation of TLM contact resistance measurements on crystalline silicon solar cells, *Sol. Energy* 151 (2017) 163–172.
- [19] S. Duttagupta, F. Ma, B. Hoex, T. Mueller, A.G. Aberle, Optimised antireflection coatings using silicon nitride on textured silicon surfaces based on measurements and multidimensional modelling, *Energy Procedia* 15 (2012) 78–83.
- [20] Z.C. Holman, A. Descoeuilles, L. Barraud, F.Z. Fernandez, J.P. Seif, S. De Wolf, C. Ballif, Current losses at the front of silicon heterojunction solar cells, *IEEE J. Photovoltaics* 2 (2012) 7–15.
- [21] Q. Hu, Z.X. Deng, L.B. Liu, L.G. Zhang, P.J. Masset, Experimental investigation of phase equilibria in the Al–Ag–Si system, *Calphad* 83 (2023).
- [22] G. Xing, W. Chen, H. Tang, X. Chen, B. Feng, H. Li, Z. Sun, Y. Wang, X. Du, Y. Liu, Al–Si contact formation involving back surface field and voids of PERC, *Sol. Energy Mater. Sol. Cells* 245 (2022).
- [23] T. Lauermann, B. Fröhlich, G. Hahn, B. Terheiden, Diffusion-based model of local Al back surface field formation for industrial passivated emitter and rear cell solar cells, *Prog. Photovolt. Res. Appl.* 23 (2015) 10–18.
- [24] Q. Wang, W. Wu, Y. Li, L. Yuan, S. Yang, Y. Sun, S. Yang, Q. Zhang, Y. Cao, H. Qu, N. Yuan, J. Ding, Impact of boron doping on electrical performance and efficiency of n-TOPCon solar cell, *Sol. Energy* 227 (2021) 273–291.
- [25] C. Reichel, R. Müller, F. Feldmann, A. Richter, M. Hermle, S.W. Glunz, Influence of the transition region between p- and n-type polycrystalline silicon passivating contacts on the performance of interdigitated back contact silicon solar cells, *J. Appl. Phys.* 122 (2017).
- [26] Q. Wang, H. Peng, S. Gu, K. Guo, W. Wu, B. Li, L. Li, N. Yuan, J. Ding, High-efficiency n-TOPCon bifacial solar cells with selective poly-Si based passivating contacts, *Sol. Energy Mater. Sol. Cells* 259 (2023).